Acta Materialia 145 (2018) 278–289

Contents lists available at ScienceDirect

Acta Materialia

journal homepage: www.elsevier.com/locate/actamat

Full length article

Meridian crack test strength of plasma-sprayed amorphous and nanocrystalline ceramic microparticles

Václav Pejchal [a, *], Marta Fornabaio [a], Goran Žagar [a], Grégory Riesen [a], Romain G. Martin [a], Jan Medřický [b], Tomáš Chráska [b], Andreas Mortensen [a]

[a] Laboratory of Mechanical Metallurgy, Institute of Materials, École Polytechnique Fédérale de Lausanne (EPFL), Station 12, CH-1015 Lausanne, Switzerland
[b] Department of Materials Engineering, Institute of Plasma Physics CAS, v.v.i., Za Slovankou 3, 182 00 Prague 8, Czech Republic

ARTICLE INFO

Article history:
Received 29 August 2017
Received in revised form
2 December 2017
Accepted 3 December 2017
Available online 21 December 2017

Keywords:
The meridian crack test
Particle strength
Plasma-spraying
Nano-ceramic
Alumina-zirconia-silica

ABSTRACT

We implement the meridian crack test method to measure the surface and subsurface flaw-controlled strength of spherical near-eutectic plasma-sprayed alumina-zirconia-silica particles of average diameter near 30 μm. The particles are tested in two states, namely as-sprayed amorphous, or nanocrystalline as obtained after a supplementary annealing step. The test consists in uniaxial compression testing of individual particles between a pair of elasto-plastic steel platens, the hardness of which is tailored to achieve relative contact radii (defined as the ratio between the radius of the projected particle-platen contact area to the particle radius) above 0.6 at the moment of particle failure. Results show that nanocrystalline particles exhibit characteristic Weibull strength 1490 MPa, which is approximately 30% higher than for amorphous particles while the Weibull modulus is, relative to the test precision, comparable, being equal to 6.0 and 7.8 for nanocrystalline and amorphous particles, respectively. This result is an indication that the flaw size distribution is not significantly affected by the annealing step, the strength increase resulting from an increase in fracture toughness upon nanocrystallisation. This conclusion is consistent with fractographic observations. The principal strength-limiting defects identified for both amorphous and nanocrystalline particles were micropores formed during plasma spraying.

1. Introduction

Microscopic ceramic particles are used to reinforce a wide range of composite materials, the mechanical properties of which are largely determined by the intrinsic strength distribution of the reinforcing particles. In brittle (e.g., ceramic) matrix composites, crack-growth resistance is improved by reinforcing the matrix with ceramic micro-particles that interact with the crack front and serve as points of crack deflection and pinning [1–6] and contribute to crack bridging [7,8]: the efficiency of both deflection and crack bridging is predicted to be more efficient for stronger particles [8–12]. In particle reinforced ductile (e.g., metal) matrix composites, the importance of particle strength is even more apparent, since particle fracture is the most frequent mechanism driving composite failure [13–23]. In tension, poor reinforcement strength leads to damage accumulation in the composite, leading to decreased composite ductility and tensile strength [24–29]. The fracture toughness of metal matrix composites is also documented to be significantly improved when stronger reinforcing ceramic particles are used [30,31]. In short, if particles with strengths approaching those of state-of-the-art high-strength ceramic fibres were used as reinforcements, remarkably strong and tough isotropic metal matrix composites could be made [25,32].

Yet, important as the intrinsic strength of microscopic reinforcing particles may be, very little is known of this quantity: there are only a few articles in which microscopic particles used as reinforcements in composites have been tested for their fracture strength; Refs. [33–36] are noteworthy exceptions. One strategy to test microscopic particles is to combine focused ion beam milling (FIB) techniques with micromechanical testing methods. Mueller et al. and Feilden et al. [35] tested the flat portion of individual silicon and alumina platelets FIB machined into the form of a bar in a microscopic three-point bending set-up using a nanoindentation device. In another study probing the microscopic strength of hard and brittle microparticles, Pejchal et al. and Mueller et al. [37,38], have tested polyhedral and plate-like alumina and silicon

* Corresponding author.
E-mail addresses: vaclav.pejchal@epfl.ch, vaclav.pejchal@alumni.epfl.ch (V. Pejchal).

https://doi.org/10.1016/j.actamat.2017.12.031

microparticles by means of an adapted C-shaped sample test [39]. These experiments show that, if brittle microcrystals are free of a limited range of well-defined defects, exceptional strength values can be achieved, as is the case with high-perfection ceramic whiskers. These testing methods require, however, access to the focused ion beam and use of high-precision (in some cases *in-situ* SEM) micromechanical testing equipment.

A different strategy to probe the intrinsic strength of microparticles is uniaxial compression; this method is widely used in other contexts to measure the strength of hard and brittle grains or particles across all length-scales [40–42]. As concerns strong particles with potential use as composite reinforcement, this approach was used by Yoshida, Ogiso et al. [33,34] and Rosenflanz et al. [36]. These authors used a pair of hard (diamond or sapphire) platens to crush individual microscopic α-alumina Sumicorundum or spheroidized amorphous and nanocrystalline rare-earth aluminate particles, respectively. Resulting fracture loads were then used to estimate the particle strength using a simple (but debatable) formula, giving mean particle strength values around 2.5 GPa and 1.8 GPa for Sumitomo alumina or nanocrystalline aluminate particles, respectively. These values are of the right order of magnitude; however, the interpretation of strength measurement methods in which a test piece is compressed diametrically between a pair of hard platens is subject to caution, as initiation and growth of extrinsic flaws near the platen-particle contact area has been repeatedly reported when hard diamond platens are used [43–48]. To circumvent this problem, the use of soft (relative to the particle) elastoplastic platens was proposed by Shipway and Hutchings [49]; in the present work we use a recent adaptation of their approach, which we call the Meridian Crack Test (MCT) method [50]. In this approach, soft (relative to the particle) elasto-plastic platens are used to achieve platen-particle contact areas much larger than in the conventional uniaxial compression test. As a result, the high stress concentration in the area along which compressive loads are applied is significantly reduced.

An interesting feature of the test is that trajectories of the tensile stress in the center and along the surface of a particle during the test are different: at a certain moment of the test the surface stress becomes dominant and is the only local stress that is still increasing as loading continues, allowing to conclude in such cases that fracture originated at a surface flaw. The method furthermore also enables, unlike many other test configurations, fractography and identification of strength-limiting defects.

It has been widely demonstrated that nanostructured ceramics in both bulk and fibre form can exhibit exceptional mechanical properties [51–58]. It should, therefore, be possible to produce nanostructured microparticles with strengths approaching those of today's engineering fibres for composite reinforcement. One way to produce such particles is to use thermal spraying, in which the feedstock material is introduced into a high temperature jet where it is melted and propelled in the form of droplets towards a fluid quenching medium. The resulting high cooling rates, on the order of 10^6 K/s, can be advantageously used to prepare amorphous and nanostructured microscopic particles, also of ceramics that are not strong glass formers [59,60]. In the present work we test such particles for strength, using the meridian crack testing method, to show how the intrinsic flaw-controlled strength of plasma-sprayed ceramic micro-particles based on the Al_2O_3-ZrO_2-SiO_2 ternary system can be measured, and improved.

2. Material and methods

2.1. Amorphous Eucor powder

The powder feedstock material from the ternary system Al_2O_3-ZrO_2-SiO_2 is based on the bulk cast ceramic material called Eucor™. This material has a near-eutectic composition, which was confirmed by semi-quantitative X-ray fluorescence; in the present work, the powder feedstock contained 46.5 wt% of Al_2O_3, 34.5 wt% of ZrO_2, 14.5 wt% of SiO_2, and 4.5 wt% of other oxides (of alkali and alkaline earth metals). It was previously reported that this near-eutectic composition of the material facilitates formation of amorphous phases when the molten material is rapidly solidified [61,62].

Fully crystalline, crushed and sieved, powder feedstock was plasma sprayed in air at atmospheric pressure using the hybrid water-stabilised plasma torch WSP-H 500 (IPP CAS, Prague) operating at 160 kW power. The powder was injected into the plasma jet, where individual particles were melted and thus turned into spheres. To retain the spherical shape of the particles while ensuring rapid solidification, sprayed molten particles were collected in a vessel filled with a liquid quenching medium which was positioned 300 mm downstream from the plasma torch exit nozzle. This quenching medium was of saturated water solution of boric acid, cooled down to 0 °C and mixed with ice; it was used for its high heat extraction ability. After spraying, the collected powder was rinsed with pure water to remove the residue of boric acid and then dried in an oven at 150 °C. This process resulted in fully amorphous powder of nearly spherical particles.

2.2. Nanostructured Eucor powder

To produce nanocrystalline particles, the as-sprayed (amorphous) powder was annealed in air at 1300 °C for 1 h, with heating and cooling rates of 5 °C/min. Crystalline phases were identified by X-Ray Diffraction (XRD) measurements carried out using PANalytical X'Pert Pro MPD diffractometer with a Cu K_α radiation. Scanning was performed in the 10–90° 2θ range using a step size of 0.0170° and time per step 29.210 s. Crystalline phase quantification was performed by Rietveld refinement using the X'Pert High Score Plus software with rutile as an external standard [63]. Scanning Electron Microscopy (Zeiss Merlin, Oberkochen, Germany) was used to investigate the microstructure of as-received and annealed Eucor particles. To this end, particles were dispersed in an epoxy resin made by mixing Bisphenol A diglycil ether (DGEBA, Sigma Aldrich) with Diethylenetriamin 99% (DETA Sigma Aldrich, 99%) which was then hardened to create a composite. This composite was then polished down to 1 μm polishing medium particle size and observed along its polished surface. Local chemical analyses were conducted by means of Energy Dispersive X-Ray spectrometry (EDX) with an electron acceleration voltage of 10 kV. About 20 random particles were analyzed in order to investigate possible variations in composition from particle to particle.

2.3. The meridian crack test

To measure the tensile strength of the plasma-sprayed Eucor particles we use the Meridian Crack Test method; its principle and theoretical background are published elsewhere [50]. Uniaxial compression tests were conducted using age-hardened AISI 630 steel, or AISI W1 steel in one of two different heat treatment conditions. This produced three different sets of platens namely (i) quenched AISI W1 steel tempered at 250 °C for 90 min (ii) quenched AISI W1 steel tempered at 320 °C for 90 min and (iii) AISI 630 steel age hardened at 480 °C for 60 min. The resulting average Vickers hardness of the three platen materials measured with a FM-300 (Future-tech Corp. Kawasaki, Japan) using a 0.5 kgf load were HV 710, 620 and 440 for materials (i), (ii) and (iii) respectively. The three platen materials are hereafter designated as HV700, HV600 and HV450, respectively.

Uniaxial compression tests were performed on individual particles 25–35 μm in diameter using a custom-built instrumented compression apparatus equipped with 10 N load cell and interchangeable conical tips made of the three platen materials. The cone tips were polished, to have an approximately 300 μm flat-end tip diameter serving as the upper platen. As the bottom platen, disc-shaped substrates ~10 mm in diameter and ~2 mm thick were used. Both tips and substrates were ground and polished using diamond suspensions down to 1 μm diamond particle size. Along the substrate surface a layer a few micrometers thick of soft colloidal graphite paint (Pelco®, Redding, CA, United States) was applied; its role was to retain the broken particle pieces in place after testing. Additionally, an adhesive tape (scotch-tape type) was applied and removed from the carbon-coated substrate. This left a very thin (several times thinner than the graphite paint layer) and scattered film of the tape adhesive, which helped to hold particles in place during manipulation of the particle-covered substrates prior to testing.

Individual particles were deposited using a miBot™ (Imina Technologies SA, Lausanne, Switzerland) remote-controlled micro-arm equipped with a sharp tungsten needle, using the following procedure: (i) by approaching the tungsten needle over the selected particle the particle adhered to the needle under the action of electrostatic forces, (ii) the particle attached to the tip of the needle was then transferred over the carbon-coated substrate at locations featuring an adhesive film layer, which then held the particle in place. To measure its diameter 2*R*, each particle was imaged top-down under an optical microscope (Olympus Vanox model AHMT, Olympus Corporation, Tokyo, Japan) equipped with a digital camera system. Additional diameter measurements on a subset of the particles were also conducted using a scanning electron microscope (SEM) (Zeiss Merlin, Oberkochen, Germany). The optical microscopy diameter measurements were found to be within 5% of electron microscopy measurements.

Particles were compressed by displacing the flat-end conical tip using a constant displacement-rate of 1 μm/s. The test was interrupted either when a load drop was recorded or, with particularly strong particles that embedded completely into the platens, when the two platens contacted. Relative error on load readings was below 1%. Each flat-end conical tip was used to test approximately 5 particles before it was changed, so that each particle was compressed by a new, flat and polished, portion of the tip surface. Indents left by tested particles in the flat surface of the conical tip were subsequently imaged using an optical microscope (Zeiss™ Axioplan 2, Oberkochen, Germany) equipped with a digital camera to measure the contact radius at the moment of failure, *a*, with an estimated relative error of 5%. Tested fractured particles were then imaged in the SEM with a goal to identify the strength-limiting defects.

3. Results

3.1. Eucor particles microstructure

The plasma spraying technique that was used to produce the particulate Eucor material resulted in particles of high sphericity and with a broad size range, diameters ranging from a few micrometers to several tens of micrometers. To check whether the particle shape was close to that of a sphere, 2230 polished random as-sprayed particle cross-sections were imaged via SEM and their periphery fitted to an ellipse. It was found that the average ellipse aspect ratio, defined as the ratio of its minor to its major axes, was 0.92, showing that the particle shape is, for a majority of the particles, nearly spherical. A small fraction (<5%) of those particles exhibited aspect ratio values below 0.7; these particles furthermore contained crystalline regions, which were observable in the SEM along the polished cross-sections. It is thus likely that those 5% of the particles had not completely melted during the plasma-spraying process.

Scanning electron microscopy (SEM) micrograph of as-sprayed Eucor particles after sieving through a 45 μm pore size sieve is shown in Fig. 1a. XRD analysis (Fig. 1b) of as-sprayed Eucor particles shows that they are almost completely amorphous with a relative amorphous phase content of 85 wt% according to Rietveld refinement analysis. The SEM micrograph in Fig. 2a displays the cross-section of a typical (spherical) as-sprayed particle; there is no apparent chemical contrast, indicating a high-homogeneity of the composition within the particle. Compositional homogeneity within this particle was confirmed with EDX analysis performed at different spots of the particle cross-section. EDX performed on 20 randomly selected particles revealed some variation in composition from particle to particle, with average values and standard deviations across the particles of the chemical elements equal to (20.0 ± 1.3), (6.9 ± 0.5) and (3.2 ± 1.2) at% for Al, Zr and Si, respectively, and oxygen atoms representing the remainder.

After annealing particles at 1300 °C for 60 min the powder becomes fully crystalline, as shown by XRD analysis (Fig. 1b) revealing mullite, tetragonal and monoclinic zirconia as primary phases.

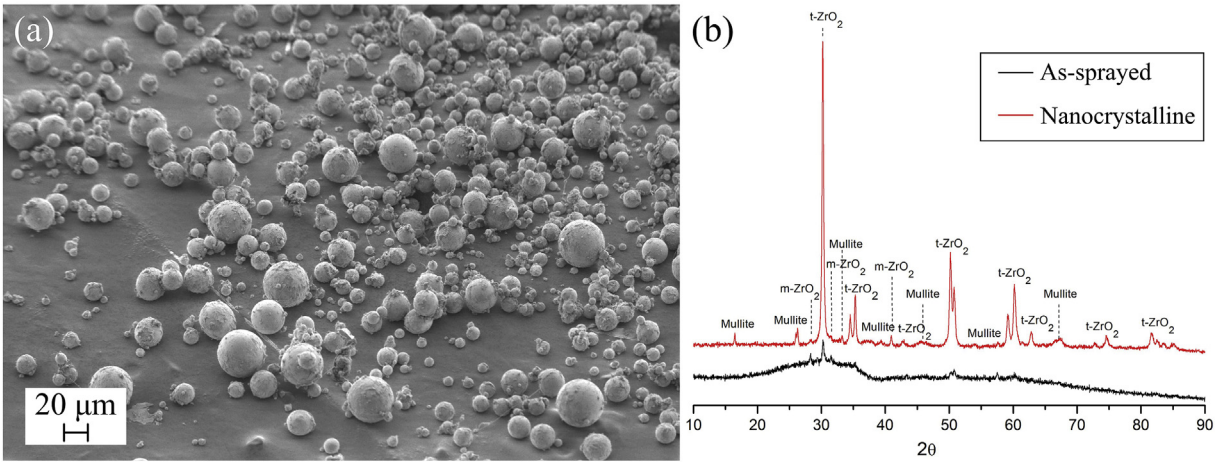

Fig. 1. (a) Overview of as-sprayed Eucor particles after sieving through 45 μm sieve. (b) XRD pattern of (black) as-sprayed and (red) annealed powder. t = tetragonal, m = monoclinic. (For interpretation of the references to colour in this figure legend, the reader is referred to the Web version of this article.)

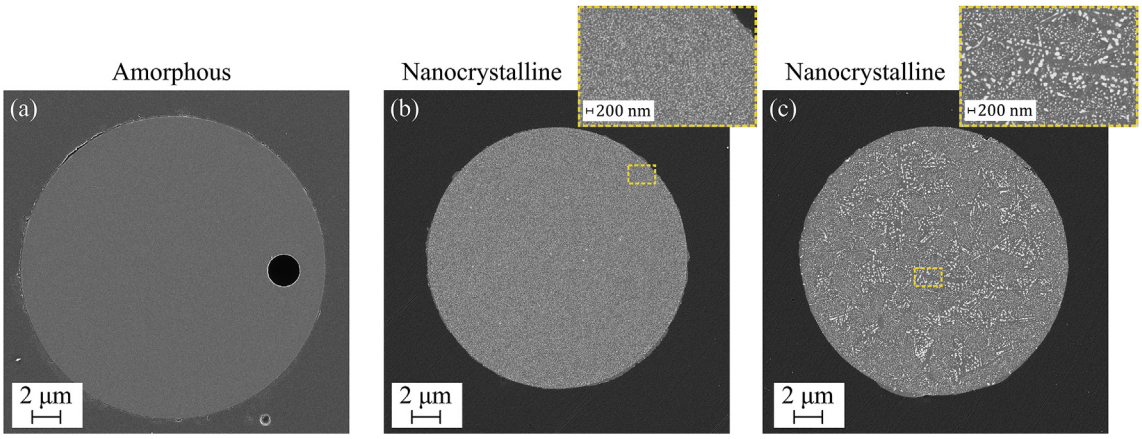

Fig. 2. (a) SEM micrograph of polished cross-section of as-sprayed amorphous Eucor particles. Panel (a) shows an amorphous particle. Panels (b) and (c) are micrographs of nanocrystalline Eucor particles obtained after 1 h annealing at 1300 °C revealing nanostructured grains of (gray) mullite and (light) tetragonal and monoclinic zirconia. A micropore is evident in the cross-section of the amorphous particle (a).

These results are in good agreement with XRD analysis of plasma-sprayed coatings prepared from similar precursor material [64]. Phase quantification by Rietveld refinement established contents of 60 wt% tetragonal zirconia, 28 wt% mullite, 4 wt% monoclinic zirconia and a remaining amorphous phase representing 8 wt%. The microstructural observations in SEM (Fig. 2b–c) revealed grains of two phases with an apparent chemical contrast; (dark-gray) mullite and (light-gray) grains of tetragonal and/or monoclinic zirconia. Two main microstructural morphologies were observed: (i) particles of very fine microstructure with equiaxed grains a few nanometers to a few tens of nanometers in size (Fig. 2b) and (ii) particles of coarser microstructure featuring a mixture of equiaxed and needle-like grains from a few tens of nanometers to a few hundred nanometers in size (Fig. 2c). In all cases mullite grains appeared as the matrix phase. EDX analyses performed on 20 polished nanocrystalline particles showed similar variations in chemical composition among particles as were found within the as-sprayed powder: averaged values and corresponding standard deviations for Al, Zr and Si chemical elements were (19.4 ± 1.1), (7.4 ± 1.4) and (3.4 ± 1.7) at%, respectively. Annealing of the powder did not lead to a formation of evident flaws (such as microcracks that might be caused by anisotropic or differential thermal expansion of the various phases present). Micropores were on the other hand readily observed in numerous particle cross-sections of both amorphous (Fig. 2a) and nanocrystalline particles.

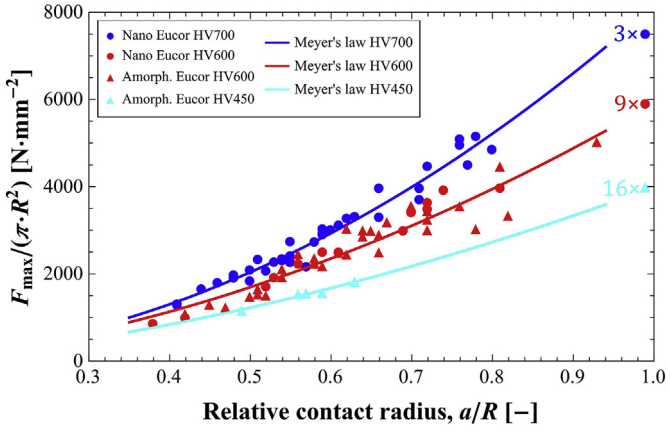

Fig. 3. Experimentally measured values of the critical force at failure normalized by the cross-sectional area of the tested particle, $F_{max}/(\pi.R^2)$ for (triangles) amorphous and (circles) nanocrystalline Eucor particles tested with (blue) HV700, (red) HV600, and (cyan) HV450 platens, respectively. Solid lines represent best fit with the power-law function $f(a/R) = k(a/R)^n$ representing the platen material Meyer's law. Values of the fitted parameters were (blue) $k = 8150$, $n = 2$ for HV700 platens, (red) $k = 5900$ and $n = 1.8$ for HV600 platens, and (cyan) $k = 3990$, $n = 1.7$ for HV450 platens. (For interpretation of the references to colour in this figure legend, the reader is referred to the Web version of this article.)

3.2. Uniaxial compression

In total, fifty-four (54) amorphous Eucor particles were tested using HV600 (33 particles) and HV450 (21 particles) platens. Of nanocrystalline Eucor, sixty-two (62) particles were tested using HV700 (40 particles) and HV600 (22 particles) platens. The average diameter of particles selected for testing was 29.7 μm and 29.9 μm and ranged between 23.1-34.7 μm and 24.5–35.5 μm for amorphous and nanocrystalline particles, respectively.

The results are summarized in Fig. 3 where the force at failure, F_{max}, normalized by the particle cross-sectional area πR^2 is plotted against the relative particle-platen contact radius a/R, where a is the contact area radius and R that of the particle. Particles that did not fail during the test and hence survived until platens contacted ($a/R \approx 1$) are indicated with a symbol at the far right of the figure. For these particles, the value of $F_{max}/(\pi R^2)$ is not representative since the measured force when $a/R \cong 1$ is affected by platens being in contact; therefore, a figurative value was selected to visualize these events in the figure to its far right.

The plot was then used to determine the elasto-plastic behavior of each platen material (HV700, HV600, and HV450). We used the relatively simple empirical Meyer law (see Ref. [65] for more information): $F_{max}/(\pi R^2) = k(a/R)^n$ where k and n are parameters characteristic of the indented material. This law has been shown in our earlier work in Ref. [50] to provide a suitable descriptor of the contact radius as function of the compressive force. Fitting the data, the estimated Meyer law parameters were $k = 8150$, $n = 2$ for HV700 platens, $k = 5900$ and $n = 1.8$ for HV600 platens, and $k = 3990$, $n = 1.7$ for HV450 platens. Note that data for particles that did not break during uniaxial compression until platens contacted were not considered for platen Meyer law determination (due to lack of precision in the force when $a/R \cong 1$).

3.3. Fractography

Fig. 4 and Fig. 5 show representative specimens of tested amorphous and nanocrystalline Eucor particles, respectively. As

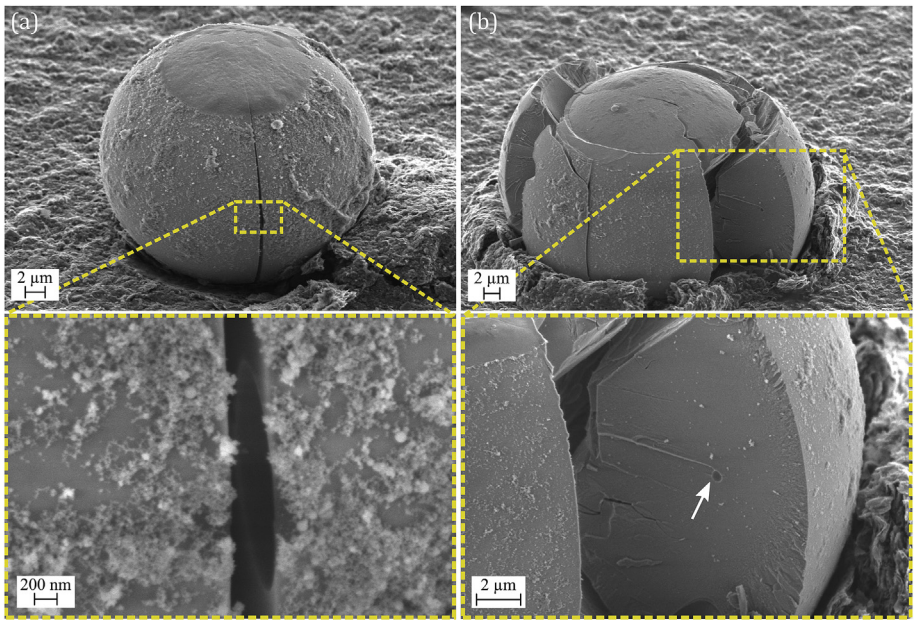

Fig. 4. SEM images of amorphous Eucor particles after uniaxial compression, illustrating particles for which distinct flaws were observed at one of the meridional cracks. (a) One meridional crack was observed for this particle, which broke at relatively low load. A pore of diameter ≈ 1 μm was observed just below the surface on the meridional crack surface. (b) The mirror-mist and hackle fractographical features point to a subsurface pore as the origin of failure. The fracture surface of amorphous Eucor particles is typically very smooth and featureless in the "mirror" region close to the origin of failure.

seen, the soft colloidal graphite layer was effective in retaining pieces of broken particles after their failure; using such particles, flaws present on one of the meridian cracks were observed. Particles were typically broken into several pieces indicating initiation and growth of secondary cracks, likely due to the sudden release of stored elastic energy after initial crack formation. The number of fragments typically scaled with the maximum load at which the particle broke. Only in the case when particles broke for low loads were one or few meridional cracks present, with the rest of the particle intact.

Fig. 4a shows a particle for which only one meridional crack was found after failure, with an evident surface pore present. Given that the first principal stress along the surface is the hoop stress, σ_ϕ, where ϕ is the azimuthal angle and peaks at the equatorial plane, the observed pore on the meridional crack fracture surface close to the equatorial plane is the likely cause of failure at low load of this

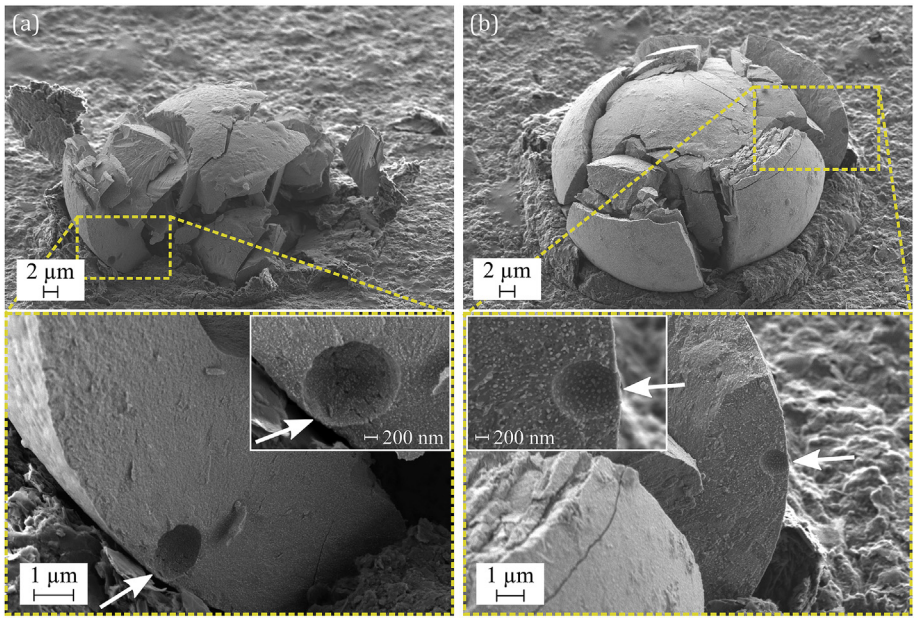

Fig. 5. SEM images of nanocrystalline Eucor particles after uniaxial compression. Panels (a), (b), illustrate two different particles for which mirror-mist-hackle patterns surrounding a pore present at one of the meridional crack fracture surfaces can be observed. In each case a surface pore was identified as the origin of failure. The fracture surface exhibits greater roughness compared to amorphous particles (Fig. 4). The grain structure is revealed on fracture surfaces, showing transgranular fracture of mullite grains (gray) and intergranular decohesion of zirconia grains (bright) close to the fracture initiation point (panel (b)).

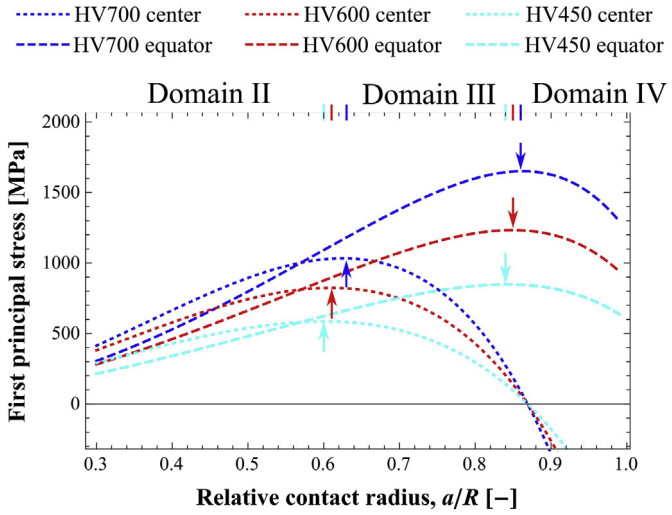

Fig. 6. Average (tensile) stress trajectories during uniaxial compression of spherical particles with Poisson's ratio 0.28, particle-platen friction coefficient 0.28 and tested with (blue) HV700, (red) HV600, and (cyan) HV450 platens calculated using Eqs. (5)–(6). The stress trajectories are plotted for (dotted) the center of the particle and (dashed) the particle surface equator versus the relative contact radius. Arrows indicate maxima for each stress trajectory and as such represent boundaries (in terms of a/R) between different Domains. (For interpretation of the references to colour in this figure legend, the reader is referred to the Web version of this article.)

particle (even though this particle broke at a/R within Domain II, see Discussion).

Other examples of pores that one can trace as likely origins of failure are shown in Fig. 4b for an amorphous particle and in Fig. 5a–b and Figure S1b in the Supplementary material for nanocrystalline Eucor particles. Distinct mirror-mist and hackle features surrounding pores are located on one of the meridional cracks close to the peak of the surface stress, making these pores the likely cause of failure of those particles. A surface or subsurface pore was determined as the failure origin in all investigated particles when a clear mirror-mist-hackle pattern could be observed on one of the meridional cracks, with one exception shown in Figure S1a in the Supplementary material. For this amorphous particle, fractographical features suggest that a surface inclusion was the failure origin.

The fracture surface of amorphous (Fig. 4a–b) Eucor particles was very smooth and featureless in the mirror region of the fracture surface. As expected, fracture surfaces of nanocrystalline Eucor particles exhibited higher roughness compared to amorphous particles. From higher magnification micrographs (Fig. 5b) one can observe the grain structure of nanocrystalline particles. A closer look at the pore surface in Fig. 5a reveals the presence of microcracks along the pore free surface. Close to the failure origin a mixed trans- and inter-granular crack path can be observed (Fig. 5b). Grain cleavage is dominant for mullite grains (dark-gray) while intergranular decohesion, leaving protruding grains and pore-like features along the fracture surface, is evident for zirconia grains. This indicates the presence of effective crack deflection by zirconia grains.

4. Discussion

4.1. The meridian crack test evaluation

A solution for the stress distribution within a linear elastic sphere diametrically compressed between a pair of platens was given by Hiramatsu and Oka [41], and was recently refined using finite element calculations in Ref. [66]. During the compression test, the relative contact radius a/R gradually increases and the peak of the tensile first principal stress, considered here as the fracture stress, is located for large enough relative contact radius ($a/R > 0.3$) either in the center of the sphere, σ_{1c} or in the particle surface equatorial belt, σ_{1s} [50]. The tensile first principal stress in the sphere center and equatorial belt can be expressed as

$$\sigma_{1c} = \frac{F}{\pi R^2} \cdot \tilde{\sigma}_{1c}\left(\frac{a}{R}, \nu, \mu\right) \tag{1}$$

$$\sigma_{1s} = \frac{F}{\pi R^2} \cdot \tilde{\sigma}_{1s}\left(\frac{a}{R}, \nu, \mu\right) \tag{2}$$

respectively, where F is the compressive force applied to the particle, R is the particle radius and $\tilde{\sigma}_{1c}, \tilde{\sigma}_{1s}$ are adimensional functions of the relative contact radius a/R, where a is the radius of the projected particle-platen contact area, ν is particle's Poisson's ratio, and μ is the friction coefficient in the particle-platen contact. The adimensional functions $\tilde{\sigma}_{1c}, \tilde{\sigma}_{1s}$ for different values of the three variables can be found in Ref. [66]. Details of the friction and Poisson's ratio estimation are given in the Supplementary Information. The (kinematic) friction coefficient was found to be approximately $\mu = 0.28$. The particle Poisson's ratio was estimated to be approximately equal $\nu = 0.28$ for both amorphous and nanocrystalline Eucor particles (that ν and μ are equal is a coincidence). For values $\nu = 0.28$ and $\mu = 0.28$ functions $\tilde{\sigma}_{1c}, \tilde{\sigma}_{1s}$ from Ref. [66] read

$$\tilde{\sigma}_{1c} = 0.623 + 0.062\left(\frac{a}{R}\right) - 0.837\left(\frac{a}{R}\right)^2 - 0.202\left(\frac{a}{R}\right)^3 + 0.508\left(\frac{a}{R}\right)^4 - 0.409\left(\frac{a}{R}\right)^5 \tag{3}$$

$$\tilde{\sigma}_{1s} = 0.429 - 0.036\left(\frac{a}{R}\right) + 0.189\left(\frac{a}{R}\right)^2 - 1.092\left(\frac{a}{R}\right)^3 + 1.563\left(\frac{a}{R}\right)^4 - 0.903\left(\frac{a}{R}\right)^5 \tag{4}$$

Knowing the platen empirical elasto-plastic indentation behavior as described by Meyer's law (Fig. 3) and combining this with Eqs. (1)–(2) one can calculate and plot *average* stress trajectories in particles compressed between platens of a given steel as a function of the relative contact radius:

$$\sigma_{1c} = k \cdot \left(\frac{a}{R}\right)^n \cdot \tilde{\sigma}_{1c} \tag{5}$$

$$\sigma_{1s} = k \cdot \left(\frac{a}{R}\right)^n \cdot \tilde{\sigma}_{1s} \tag{6}$$

Fig. 6 presents the evolution of the first principal stress at the center, and along the surface equatorial belt of a particle, versus the relative contact radius, with $\nu = 0.28$ and $\mu = 0.28$ during uniaxial compression using HV700, HV600 or HV450 steel platens. As described in Ref. [50] four different domains can be defined:

(i) the contact stress dominated Domain I starts from the beginning of the test ($a/R = 0$) and extends until a/R is approximately equal to 0.3 (not plotted here as no particle failed in this domain),
(ii) Domain II starts at $a/R \approx 0.3$ and is a region where tensile stress peaks in the central portion of the particle. As compression continues, a/R increases and central and surface stresses increase simultaneously;

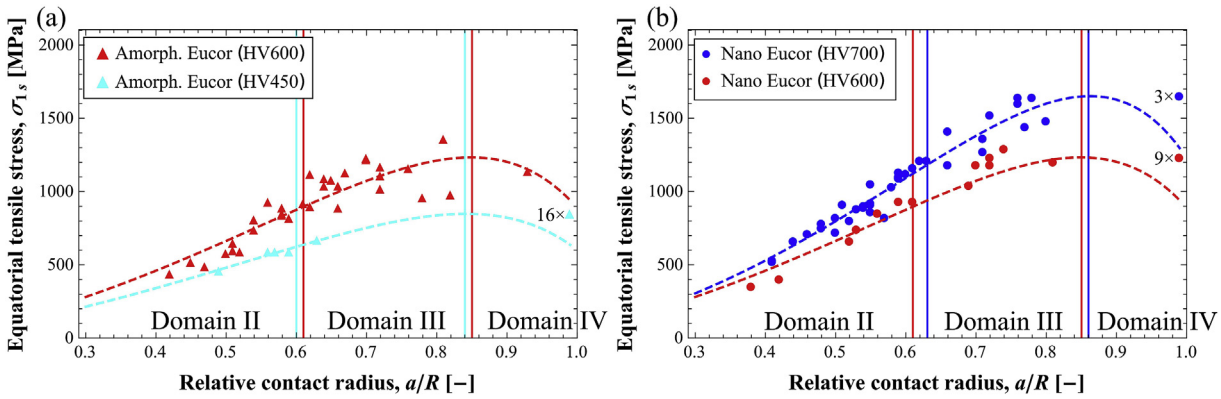

Fig. 7. Surface equatorial stress at the moment of failure for tested particles versus the relative contact radius a/R for (a) amorphous and (b) nanocrystalline Eucor particles. Dashed lines represent the average stress trajectories and solid vertical lines represent predicted boundaries between Domains III and IV for given platens. Symbols at the far right represent particles that survived until platens contacted.

(iii) the stress in the particle center then peaks, leading to a transition into Domain III where it is only within the surface equatorial belt that the tensile stress continues to increase as compression progresses; elsewhere stress values have started to decrease;
(iv) finally, Domain IV is characterized by tensile stresses decreasing everywhere in the compressed sphere, including along the surface equatorial belt.

The boundary between Domains II and III was here defined as the moment (in terms of a/R) when the first principal stress in center reaches its maximum value, i.e. $\frac{d\sigma_{1c}}{d(a/R)} = 0$. In our previous work with fused quartz particles [50], the boundary between Domain II and III was defined as the crossover between the center and surface equator stress trajectories: the reason for the difference is that with particles of higher Poisson ratio compared to that of fused quartz, such as the nanocrystalline Eucor tested here, the crossover between the central and equator stress is located slightly before the central stress reaches its maximum value (see Fig. 6).

While tensile stresses increase simultaneously both in central and surface regions (Domain II) particle failure may occur either in the particle center or along its surface, with the central and surface stress values differing by up to roughly 40%. If a particle breaks within Domain III, i.e., after the central stress reaches its peak, then the only region where the tensile stress is still increasing is around its equatorial belt and the surface equatorial stress; σ_{1s}, can therefore be considered as the particle failure stress. Note that beyond a certain point ($a/R \sim 0.85$) the stress in the sphere center σ_{1c} becomes compressive.

One can observe failure events in Domain III only for particles that are sufficiently strong to enter it. Failure events in Domain III are therefore, in the language of survival analysis, left-truncated (only values for the strength of particles stronger than a certain value can be observed). The left-truncation value σ_T depends on the platen material and can be estimated from the curves of the average stress trajectories (Fig. 6) as the stress value at which Domain III begins. There is, however, scatter in data points used to derive Meyer's law (Fig. 7). For this reason, some of the measured surface strength values (computed knowing a/R from the measured load) of data points situated, according to the value of a/R, in Domain III may be slightly lower than the σ_T value determined from the average stress trajectory curves (Fig. 6). Therefore, the lower of the two values determined as (i) the surface equatorial stress σ_{1s} for the a/R value at which $\frac{d\sigma_{1c}}{d(a/R)} = 0$ from the average stress trajectory curves and (ii) the lowest actual measured strength value ascertained to be, by its value of a/R, in Domain III (lowered by a negligible value namely 1 MPa as the observed value cannot be equal to the left-truncation value) was taken as σ_T. To observe failure events of weaker particles in Domain III (i.e. to decrease the left-truncation value) one has to decrease the hardness of the used platens.

If a particle is strong enough to (in the language of survival analysis) *survive* the maximum attainable stress in the equatorial belt of Domain III, it enters Domain IV. The boundary between Domains III and IV is defined as value of a/R at which the tensile stress in the surface equatorial belt reaches its maximum, i.e. $\frac{d\sigma_{1s}}{d(a/R)} = 0$. Particles that have entered Domain IV cannot in principle break anymore since, according to mechanical analysis, the tensile stress decreases thereafter everywhere in the sphere. One therefore only knows a lower-bound of the strength of such particles; in Survival analysis terminology, the stress at this transition is a *right-censoring* stress value, σ_C. This value is found as the maximum on the average equatorial stress trajectory curve, for a given platen material (Fig. 6).

The a/R values representing boundaries between Domains are indicated in Fig. 6 with arrows and are listed in Table 1. The left-truncation and right-censoring values for each platen-particle material combination used in this work obtained from Fig. 6 and from experimental data points (Fig. 7) are also listed in Table 1. For a more detailed description of Survival analysis tools used here, readers are referred to Ref. [50] and to the clear and user-friendly overview provided in Ref. [67].

Measured experimental values of the stress in the equatorial belt of each tested particle according to Eq. (2) together with the average stress trajectory Eq. (6) are shown in Fig. 7. With amorphous Eucor particles, 18 particles tested with HV600 platens and 1 particle tested with HV450 platens failed in Domain III. One particle tested with HV600 platen entered Domain IV and failed later on. When tested with HV450 platens 16 particles survived until platens contacted (Domain IV).

Table 1
Values of the relative contact radius a/R at the beginning and end of Domain III for tested amorphous and nanocrystalline Eucor particles ($\nu = 0.28$, $\mu = 0.28$) and the tensile stress values identified as the left-truncation, $\boldsymbol{\sigma_T}$, and right-censoring, $\boldsymbol{\sigma_C}$ values.

Platen material	Domain III start		Domain III end	
	a/R	$\boldsymbol{\sigma_T}$ (MPa)	a/R	$\boldsymbol{\sigma_C}$ (MPa)
HV700	0.63	1030	0.86	1650
HV600	0.61	820	0.85	1230
HV450	0.60	590	0.84	850

Table 2
Ensemble of the Domain III and IV results used to calculate the surface stress survival probability.

Amorphous Eucor				Nanocrystalline Eucor			
Platen	Measured failure/censoring peak surface stress [MPa]	Censoring indicator[a]	Left-truncated at σ_T =[MPa]	Platen	Measured failure/censoring peak surface stress [MPa]	Censoring indicator[a]	Left-truncated at σ_T = [MPa]
HV600	1110	0	820	HV700	1180	0	1030
	1130	0	820		1410	0	1030
	900	0	820		1440	0	1030
	890	0	820		1480	0	1030
	1170	0	820		1520	0	1030
	920	0	820		1270	0	1030
	1040	0	820		1210	0	1030
	1230	0	820		1600	0	1030
	1360	0	820		1360	0	1030
	1160	0	820		1640	0	1030
	1080	0	820		1640	0	1030
	960	0	820		1650	1	1030
	1220	0	820		1650	1	1030
	980	0	820		1650	1	1030
	1020	0	820	HV600	1230	0	820
	1090	0	820		930	0	820
	1120	0	820		1180	0	820
	1040	0	820		1290	0	820
	1230	1	820		1180	0	820
HV450	670	0	590		1200	0	820
	850	1	590		1040	0	820
	850	1	590		1230	1	820
	850	1	590		1230	1	820
	850	1	590		1230	1	820
	850	1	590		1230	1	820
	850	1	590		1230	1	820
	850	1	590		1230	1	820
	850	1	590		1230	1	820
	850	1	590		1230	1	820
	850	1	590		1230	1	820
	850	1	590				
	850	1	590				
	850	1	590				
	850	1	590				
	850	1	590				
	850	1	590				

[a] when 0, the surface stress represents the surface strength measurement, otherwise value 1 indicates right-censoring and the value in the surface stress column represents a lower-bound of the surface strength.

For nanocrystalline Eucor particles, 11 particles failed in Domain III when tested with HV700 platen and 7 particles tested with HV600 platens. Three particles tested with HV700 and 9 particles tested with HV600 platens survived until platens contacted (thus entering Domain IV).

The reason why one particle failed in Domain IV might be explained by slow-crack-growth, as was proposed for particles in Ref. [50]; alternatively it can represent an outlier for which the transition between Domains III and IV was far off the predicted value. In collating particle strength data, this particle was considered to have survived the right-censoring value, σ_C of the platen that it was tested with (HV600). The ensemble of the surface failure events (Domain III) and events for which we only know the right-censored value and all data that were left-truncated for the value of Domain III beginning for the corresponding platen are presented in Table 2.

4.2. Surface strength distribution

Fig. 8 shows estimated survival distribution using (i) the non-parametric Kaplan-Meier product-limit estimator and (ii) the two-parameter Weibull distribution using the data from Table 2. The two survival distributions were estimated with the Wolfram Mathematica 10.1 (Wolfram Research, Inc, USA) computation program using incorporated functions *SurvivalModelFit* and *EstimatedDistribution* for product-limit estimator and Weibull distribution parameter estimation, respectively. Plotting the non-parametric and parametric estimations over one another shows that they are mutually consistent. The estimated Weibull modulus m and the

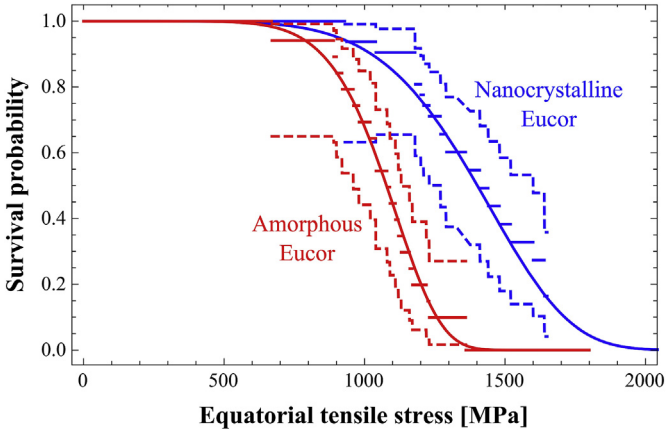

Fig. 8. Survival probability of (red) amorphous and (blue) nanocrystalline Eucor particles with respect to the surface equatorial stress evaluated from Domain III and IV events. (continuous solid lines) two parameter Weibull distribution, (stepped lines) Kaplan-Meier product-limit estimator, (dashed stepped lines) 95% confidence intervals for the Kaplan-Meier estimation. (For interpretation of the references to colour in this figure legend, the reader is referred to the Web version of this article.)

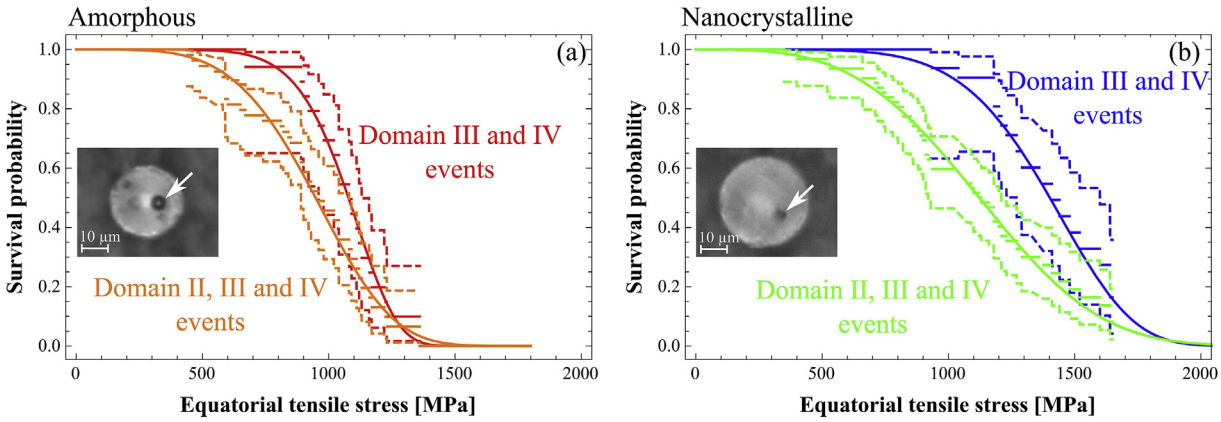

Fig. 9. Comparison of the surface equatorial stress survival distribution of (a) amorphous and (b) nanocrystalline Eucor particles obtained using events from Domains III and IV and Domains II, III and IV where failure events from Domain II are considered all to be due to the surface stress. Two optical microscopy pictures represent amorphous and nanocrystalline particles observed before testing and which failed at relatively low loads in Domain II: one notices the presence of micrometric pores near the particle center. These (a) amorphous and (b) nanocrystalline particles failed for central stress values $\sigma_{1c} = 580$ **MPa** and $\sigma_{1c} = 660$ **MPa**, respectively.

characteristic strength (scale parameter) σ_0 are $m = 7.8 \pm 1.5$ and $\sigma_0 = (1130 \pm 30)$ MPa for amorphous Eucor particles, and $m = 6.0 \pm 1.3$, $\sigma_0 = (1490 \pm 70)$ MPa for the nanocrystalline Eucor particles. The standard error in the parameter estimation was assessed using a bootstrapping technique; specifics are presented in the Supplementary Information.

In order to assess the effect of uncertainty in the Poisson's ratio estimation on results, we have reevaluated the data with two extreme values of the expected particle's Poisson's ratio, namely 0.25 and 0.3. Changing the particle Poisson's ratio ν had little effect on the Weibull modulus results; this is owing to the fact that the Domain's boundaries in a/R terms are not sensitive to the exact value of ν. The value of the Poisson's ratio has, on the other hand, some effect on the scale parameter of the resulting Weibull distribution: the characteristic strength σ_0 changes within 5% relative to the value determined with $\nu = 0.28$. This difference is, however, lower than the error of the stress calculation using Eq. (2), which is approximately 5–10% [66]. The sensitivity of the Weibull parameters to the value of the friction coefficient μ is small: when μ is changed to 0.25 or 0.3 their variation is well below 5% (see Supplementary Information for details).

From Fig. 8 it is evident that, after annealing, the particle strength increases noticeably, by roughly 30% on average. The Weibull modulus decreases only slightly, which means that there is slightly more scatter in observed results; this may be attributed to the presence of slightly greater microstructural differences between individual nanocrystalline particles (Fig. 2). This difference in the scatter is, however, only marginal given the accuracy of the measured Weibull modulus.

The fact that after crystallization annealing the strength of particles increases while the Weibull modulus remains relatively unaffected suggests that observed changes in particle strength distribution are mostly the result of an increase in the fracture toughness of the material while the particles' flaw distribution remains mostly unchanged. For both types of particles, micropores produced during the powder processing by trapping air when in the molten state were linked to the fracture origin: that these would not be altered by the annealing treatment is reasonable. We thus conclude that the difference in observed strengths between amorphous and nanocrystalline particles is explained by an increase in the fracture toughness of the particle material after annealing. Nanocrystallisation apparently made the particles tougher by a value that is high enough to increase their strength by 30% or more since, as we discuss later, pores in nanocrystalline particles have likely a more detrimental effect on strength than in amorphous particles.

4.3. Strength-limiting defects

In glasses and glass ceramics it is known that the mirror region size surrounding the fracture origin can be directly linked to the fracture stress. In the amorphous particles the size of mirrors, r_m, present on meridional cracks surrounding critical flaws can thus be linked with the measured surface equatorial fracture stress if one assumes that the particle fracture toughness is in the range 0.4–1.0 MPa $m^{1/2}$ depending on the mirror-constant-to-fracture-toughness ratio used (this varies in the literature between 2.3 and 3 [68–70]). This deduced fracture toughness range is in good agreement with what one would expect for the present amorphous Eucor particles material, since it is comparable to that of silica and aluminate-glasses [71–73] (see Supplementary Information for details).

In nanocrystalline Eucor the mirror size surrounding fracture origins is less well defined. We have therefore tested whether the measured surface equatorial fracture stress can be linked with the observed surface and subsurface pores if these are assimilated to sharp penny-shape flaws. The rationale behind such an assimilation of pores for nanocrystalline particles to sharp flaws is based on observations of Rice [74], as well as our own observation of microcracking along the pore internal surface in one of the nanocrystalline particles. The measured fracture stress can then be linked with observed pores acting as sharp flaws for material with fracture toughness values in the range of 1.0–2.2 MPa $m^{1/2}$ (see Supplementary Information for details). This is again in good agreement with the expected fracture toughness of the present nanocrystalline particle material: its lower bound should be near the toughness of the amorphous powder while the upper bound should be close to that of (coarse grained) mullite (≈ 2 MPa $m^{1/2}$) [75–77] or mullite reinforced with zirconia grains, of toughness value in the range of 2.5–6 MPa $m^{1/2}$ depending on the preparation method and grains size and shape [78–80].

4.4. Data for competing center and surface failure – Domain II

A few particles failed for a/R values that situate their fracture within Domain II; these particles showed surface or subsurface

pores that could be identified as the origin of failure and were such that the pore or associated mirror size correlated well with the measured surface equatorial belt stress value for the particle in question (see Figs. S3 and S4 in Supplementary Information). We hence re-analyzed all data to probe whether *all* particle failures could have originated at a surface flaw.

We therefore assumed that all Domain II particles failed due to a flaw along their surface and included Domain II failure events, with the predicted surface equatorial stress as the failure stress, into the Survival-analysis data set of Domain III failure events (Section 4.1). Adding data points from Domain II with identified (surface) failure stress values, effectively removes any left-truncation in such event data (as Domain II starts for very low σ_{1s}). Fig. 9 compares the thus-obtained surface strength distribution with the distribution obtained by only considering data points that were within Domains III and IV (i.e., with left-truncation). The evident discrepancy between the two strength distributions shows that, at least for some of the particles that failed in Domain II, there was a failure origin other than a surface defect. Most probably there was, for some of these particles, a flaw in its central region. This is supported by observations of large (a few micrometers in diameter) pores close to the central region in several particles that failed in Domain II. Two such particles with evident pores of this type (revealed before testing by means of transmission light microscopy), are shown in Fig. 9: these two particles were among the weakest tested for amorphous and nanocrystalline Eucor, respectively (the central stress at the moment of failure for the two particles was $\sigma_{1c} = 580$ MPa and $\sigma_{1c} = 660$ MPa for the amorphous (Panel a) and nanocrystalline (Panel b) particle, respectively).

4.5. Comparison with other microscopic ceramic fibre/particle strength data

The measured surface strengths of particles from the present study are comparable to values reported for Al_2O_3-La_2O_3-Gd_2O_3-ZrO_2 (ALZG) microscopic particles, of composition 58/15/5/22 by molar ratio, tested in compression between a pair of hard (sapphire) platens [36]. Amorphous ALZG particles exhibited average strength on the order of 1100 MPa; after annealing their strength gradually increased, reaching peak average strength of 1800 MPa after a 1300 °C anneal, and decreased to approximately 1200 MPa after annealing at 1400 °C. Note that, although these strengths are comparable to values measured here, the method used (hard platens) provides strength results only for the central portion of particles; additionally, using hard platens can affect results by the nucleation of extraneous flaws along the immediate periphery of the platen/particle contact regions.

The observed microstructure and composition of present nanocrystalline Eucor particles, composed mainly of mullite reinforced with zirconia grains, are somewhat similar to those of nanocrystalline high-strength Nextel™ 720 fibres. The microstructure of these fibres is composed of mullite reinforced with nanometric alumina grains [81]. The reported Weibull strength distribution of these fibres is $m \approx 7–8$ and $\sigma_0 \approx 2000–2100$ MPa [51]. The surface strength of particles from this study thus approaches (reaching $\approx 70\%$) that of chemically and microstructurally comparable engineering fibres used as reinforcements in composites; however, the present Eucor particles cannot rival with the strongest ceramic fibres available (see Figure S5 in Supplementary Information), the reason being the deleterious influence of micropores present within the plasma-remelted powder. Removing those defects would therefore result in significantly stronger ceramic particles, with the implication that there is ample scope for the production of Eucor particles of significantly higher strength than was measured here.

5. Conclusion

We use the Meridian Crack Test method to measure the local strength of individual amorphous and nanocrystalline ceramic particles based on Al_2O_3-ZrO_2-SiO_2 eutectic ternary system and prepared using a plasma-spraying technique with Eucor™ as the feedstock powder. Results show that nanocrystalline particles obtained by annealing the amorphous powder at 1300 °C for 1 h are on average 30% stronger than amorphous particles. The Weibull modulus for nanocrystalline particles was found to be approximately 6 with a characteristic strength of 1490 MPa. Spherical pores of size ranging from few hundred nanometers to few micrometers were identified as the principal strength limiting-defects for both amorphous and nanocrystalline particles. Similar Weibull modulus values and fractographic observation suggest that the 30% increase in particle strength obtained after annealing results from an increase in the fracture toughness of nanocrystalline particles by at least 30% over that of the same particles in the amorphous state.

Acknowledgement

This research was funded by the European Research Council under the European Union's Seventh Framework Programme (FP/2007–2013)/ERC Advanced Grant Agreement No. 291085. Scanning electron microscopy was performed at the Interdisciplinary Center of Electron Microscopy at the École Polytechnique Fédérale de Lausanne (CIME-EPFL).

Appendix A. Supplementary data

Supplementary data related to this article can be found at https://doi.org/10.1016/j.actamat.2017.12.031.

References

[1] Y.-S. Chou, D.J. Green, Silicon carbide platelet/alumina composites: III, toughening mechanisms, J. Am. Ceram. Soc. 76 (1993) 1985–1992, https://doi.org/10.1111/j.1151-2916.1993.tb08321.x.
[2] D.S. King, W.G. Fahrenholtz, G.E. Hilmas, Microstructural effects on the mechanical properties of SiC-15 vol% TiB2 particulate-reinforced ceramic composites, J. Am. Ceram. Soc. 96 (2013) 577–583, https://doi.org/10.1111/jace.12091.
[3] F.F. Lange, The interaction of a crack front with a second-phase dispersion, Philos. Mag 22 (1970) 0983–0992, https://doi.org/10.1080/14786437008221068.
[4] A.G. Evans, The strength of brittle materials containing second phase dispersions, Philos. Mag 26 (1972) 1327–1344, https://doi.org/10.1080/14786437208220346.
[5] G. c. Wei, P. f. Becher, Improvements in mechanical properties in SiC by the addition of TiC particles, J. Am. Ceram. Soc. 67 (1984) 571–574, https://doi.org/10.1111/j.1151-2916.1984.tb19174.x.
[6] K.T. Faber, A.G. Evans, Crack deflection processes—II. Experiment, Acta Metall. 31 (1983) 577–584, https://doi.org/10.1016/0001-6160(83)90047-0.
[7] B. Budiansky, J.C. Amazigo, A.G. Evans, Small-scale crack bridging and the fracture toughness of particulate-reinforced ceramics, J. Mech. Phys. Solid. 36 (1988) 167–187, https://doi.org/10.1016/S0022-5096(98)90003-5.
[8] P.F. Becher, Microstructural design of toughened ceramics, J. Am. Ceram. Soc. 74 (1991) 255–269, https://doi.org/10.1111/j.1151-2916.1991.tb06872.x.
[9] K.T. Faber, A.G. Evans, Crack deflection processes—I. Theory, Acta Metall. 31 (1983) 565–576, https://doi.org/10.1016/0001-6160(83)90046-9.
[10] D.J. Green, P.S. Nicholson, J.D. Embury, Fracture of a brittle particulate composite: Part 2, J. Mater. Sci. 14 (1979) 1657–1661, https://doi.org/10.1007/BF00569287.
[11] D.J. Green, P.S. Nicholson, J.D. Embury, Fracture of a brittle particulate composite: Part 1, J. Mater. Sci. 14 (1979) 1413–1420, https://doi.org/10.1007/BF00549316.
[12] D.J. Green, Fracture toughness predictions for crack bowing in brittle particulate composites, J. Am. Ceram. Soc. 66 (1983), https://doi.org/10.1111/j.1151-2916.1983.tb09975.x. C–4.
[13] P.M. Mummery, B. Derby, C.B. Scruby, Acoustic emission from particulate-reinforced metal matrix composites, Acta Metall. Mater. 41 (1993) 1431–1445, https://doi.org/10.1016/0956-7151(93)90252-N.
[14] S. Ghosh, S. Moorthy, Particle fracture simulation in non-uniform microstructures of metal–matrix composites, Acta Mater. 46 (1998) 965–982,

https://doi.org/10.1016/S1359-6454(97)00289-9.
[15] Y. Brechet, J.D. Embury, S. Tao, L. Luo, Damage initiation in metal matrix composites, Acta Metall. Mater. 39 (1991) 1781–1786, https://doi.org/10.1016/0956-7151(91)90146-R.
[16] L. Babout, E. Maire, R. Fougères, Damage initiation in model metallic materials: X-ray tomography and modelling, Acta Mater. 52 (2004) 2475–2487, https://doi.org/10.1016/j.actamat.2004.02.001.
[17] A.B. Pandey, B.S. Majumdar, D.B. Miracle, Deformation and fracture of a particle-reinforced aluminum alloy composite: Part I. Experiments, Metall. Mater. Trans. A 31 (2000) 921–936.
[18] J.J. Lewandowski, C. Liu, W.H. Hunt Jr., Effects of matrix microstructure and particle distribution on fracture of an aluminum metal matrix composite, Mater. Sci. Eng. A 107 (1989) 241–255, https://doi.org/10.1016/0921-5093(89)90392-4.
[19] P. Scarber, G.M. Janowski, Finite element analysis of reinforcement particle cracking in Al/SiCp composites, Mater. Sci. Technol. MST Lond 17 (2001) 1339.
[20] P.M. Mummery, B. Derby, In situ scanning electron microscope studies of fracture in particulate-reinforced metal-matrix composites, J. Mater. Sci. 29 (1994) 5615–5624, https://doi.org/10.1007/BF00349956.
[21] M. Li, S. Ghosh, O. Richmond, An experimental–computational approach to the investigation of damage evolution in discontinuously reinforced aluminum matrix composite, Acta Mater. 47 (1999) 3515–3532, https://doi.org/10.1016/S1359-6454(99)00148-2.
[22] J. Llorca, J.L. Martínez, M. Elices, Reinforcement fracture and tensile ductility in sphere-reinforced metal-matrix composites, Fatig. Fract. Eng. Mater. Struct. 20 (1997) 689–702, https://doi.org/10.1111/j.1460-2695.1997.tb00301.x.
[23] J. Llorca, A. Martin, J. Ruiz, M. Elices, Particulate fracture during deformation of a spray formed metal-matrix composite, Metall. Trans. A 24 (1993) 1575–1588, https://doi.org/10.1007/BF02646597.
[24] M. Kouzeli, L. Weber, C. San Marchi, A. Mortensen, Influence of damage on the tensile behaviour of pure aluminium reinforced with ≥40 vol. pct alumina particles, Acta Mater. 49 (2001) 3699–3709, https://doi.org/10.1016/S1359-6454(01)00279-8.
[25] A. Hauert, A. Rossoll, A. Mortensen, Ductile-to-brittle transition in tensile failure of particle-reinforced metals, J. Mech. Phys. Solid. 57 (2009) 473–499, https://doi.org/10.1016/j.jmps.2008.11.006.
[26] A. Hauert, A. Rossoll, A. Mortensen, Particle fracture in high-volume-fraction ceramic-reinforced metals: governing parameters and implications for composite failure, J. Mech. Phys. Solid. 57 (2009) 1781–1800, https://doi.org/10.1016/j.jmps.2009.08.005.
[27] A. Miserez, R. Müller, A. Rossoll, L. Weber, A. Mortensen, Particle reinforced metals of high ceramic content, Mater. Sci. Eng. A 387–389 (2004) 822–831, https://doi.org/10.1016/j.msea.2004.05.054.
[28] A. Miserez, R. Müller, A. Mortensen, Increasing the strength/toughness combination of high volume fraction particulate metal matrix composites using an Al-Ag matrix alloy, Adv. Eng. Mater. 8 (2006) 56–62, https://doi.org/10.1002/adem.200500185.
[29] C. Krüger, A. Mortensen, Infiltrated Cu8Al–Ti alumina composites, Compos. Part Appl. Sci. Manuf 66 (2014) 1–15, https://doi.org/10.1016/j.compositesa.2014.06.019.
[30] A. Miserez, A. Rossoll, A. Mortensen, Fracture of aluminium reinforced with densely packed ceramic particles: link between the local and the total work of fracture, Acta Mater. 52 (2004) 1337–1351, https://doi.org/10.1016/j.actamat.2003.11.019.
[31] A. Miserez, A. Mortensen, Fracture of aluminium reinforced with densely packed ceramic particles: influence of matrix hardening, Acta Mater. 52 (2004) 5331–5345, https://doi.org/10.1016/j.actamat.2004.07.038.
[32] C. Tekoglu, T. Pardoen, A micromechanics based damage model for composite materials, Int. J. Plast. 26 (2010) 549–569, https://doi.org/10.1016/j.ijplas.2009.09.002.
[33] H. Ogiso, M. Yoshida, S. Nakano, J. Akedo, Effects of Al ion implantation on the strength of Al2O3 particles, Surf. Coating. Technol. 201 (2007) 8180–8184, https://doi.org/10.1016/j.surfcoat.2006.01.093.
[34] M. Yoshida, H. Ogiso, S. Nakano, J. Akedo, Compression test system for a single submicrometer particle, Rev. Sci. Instrum. 76 (2005), 093905, https://doi.org/10.1063/1.2038187.
[35] E. Feilden, T. Giovannini, N. Ni, C. Ferraro, E. Saiz, L. Vandeperre, F. Giuliani, Micromechanical strength of individual Al2O3 platelets, Scr. Mater 131 (2017) 55–58, https://doi.org/10.1016/j.scriptamat.2017.01.008.
[36] A. Rosenflanz, J. Tangeman, T. Anderson, On processing and properties of liquid phase derived glass ceramics in Al2O3–La2O3–ZrO2 system, Adv. Appl. Ceram 111 (2012) 323–332, https://doi.org/10.1179/1743676112Y.0000000012.
[37] M.G. Mueller, G. Žagar, A. Mortensen, In-situ strength of individual silicon particles within an aluminium casting alloy, Acta Mater. 143 (2018) 67–76, https://doi.org/10.1016/j.actamat.2017.09.058.
[38] V. Pejchal, M. Fornabaio, G. Žagar, A. Mortensen, The local strength of individual alumina particles, J. Mech. Phys. Solid. 109 (2017) 34–49, https://doi.org/10.1016/j.jmps.2017.08.005.
[39] G. Žagar, V. Pejchal, M.G. Mueller, A. Rossoll, M. Cantoni, A. Mortensen, The local strength of microscopic alumina reinforcements, Acta Mater. 100 (2015) 215–223, https://doi.org/10.1016/j.actamat.2015.08.026.
[40] W.W. Gerberich, W.M. Mook, C.R. Perrey, C.B. Carter, M.I. Baskes, R. Mukherjee, A. Gidwani, J. Heberlein, P.H. McMurry, S.L. Girshick, Superhard silicon nanospheres, J. Mech. Phys. Solid. 51 (2003) 979–992, https://doi.org/10.1016/S0022-5096(03)00018-8.
[41] Y. Hiramatsu, Y. Oka, Determination of the tensile strength of rock by a compression test of an irregular test piece, Int. J. Rock Mech. Min. Sci. Geomech. Abstr. 3 (1966) 89–99, https://doi.org/10.1016/0148-9062(66)90002-7.
[42] Y. Nakata, Y. Kato, M. Hyodo, A.F.L. Hyde, H. Murata, One-dimensional compression behaviour of uniformly graded sand related to single particle crushing strength, Soils Found. 41 (2001) 39–51, https://doi.org/10.3208/sandf.41.2_39.
[43] J.J. Swab, J. Yu, R. Gamble, S. Kilczewski, Analysis of the diametral compression method for determining the tensile strength of transparent magnesium aluminate spinel, Int. J. Fract. 172 (2011) 187–192, https://doi.org/10.1007/s10704-011-9655-1.
[44] J.A. Hudson, E.T. Brown, F. Rummel, The controlled failure of rock discs and rings loaded in diametral compression, Int. J. Rock Mech, Min. Sci. Geomech. Abstr 9 (1972) 241–248, https://doi.org/10.1016/0148-9062(72)90025-3.
[45] R. Majzoub, M.M. Chaudhri, High-speed photography of low-velocity impact cracking of solid spheres, Philos. Mag. Lett. 80 (2000) 387–393, https://doi.org/10.1080/095008300403521.
[46] M.M. Chaudhri, Impact breakage of semi-brittle spheres, Powder Technol. 143–144 (2004) 31–40, https://doi.org/10.1016/j.powtec.2004.04.006.
[47] K. Schönert, Breakage of spheres and circular discs, Powder Technol. 143–144 (2004) 2–18, https://doi.org/10.1016/j.powtec.2004.04.004.
[48] W. Wang, M.R. Coop, An investigation of breakage behaviour of single sand particles using a high-speed microscope camera, Geotechnique 66 (2016) 984–998, https://doi.org/10.1680/jgeot.15.P.247.
[49] P.H. Shipway, I.M. Hutchings, Fracture of brittle spheres under compression and impact loading. I. Elastic stress distributions, Philos. Mag. A. 67 (1993) 1389–1404, https://doi.org/10.1080/01418619308225362.
[50] V. Pejchal, G. Žagar, R. Charvet, C. Dénéréaz, A. Mortensen, Compression testing spherical particles for strength: theory of the meridian crack test and implementation for microscopic fused quartz, J. Mech. Phys. Solid. 99 (2017) 70–92, https://doi.org/10.1016/j.jmps.2016.11.009.
[51] D.M. Wilson, Statistical tensile strength of NextelTM 610 and NextelTM 720 fibres, J. Mater. Sci. 32 (1997) 2535–2542, https://doi.org/10.1023/A:1018538030985.
[52] K. Niihara, New design concept of structural ceramics, J. Ceram. Soc. Jpn. 99 (1991) 974–982, https://doi.org/10.2109/jcersj.99.974.
[53] J.D. Kuntz, G.-D. Zhan, A.K. Mukherjee, Nanocrystalline-matrix ceramic composites for improved fracture toughness, MRS Bull. 29 (2004) 22–27, https://doi.org/10.1557/mrs2004.12.
[54] Roy W. Rice, Mechanical Properties of Ceramics and Composites : Grain and Particle Effects, Marcel Dekker, New York, 2000.
[55] I.A. Ovid'ko, Micromechanics of fracturing in nanoceramics, Phil Trans R Soc A 373 (2015) 20140129, https://doi.org/10.1098/rsta.2014.0129.
[56] I. Szlufarska, A. Nakano, P. Vashishta, A crossover in the mechanical response of nanocrystalline ceramics, Science 309 (2005) 911–914, https://doi.org/10.1126/science.1114411.
[57] Y. Zhao, J. Qian, L.L. Daemen, C. Pantea, J. Zhang, G.A. Voronin, T.W. Zerda, Enhancement of fracture toughness in nanostructured diamond–SiC composites, Appl. Phys. Lett. 84 (2004) 1356–1358, https://doi.org/10.1063/1.1650556.
[58] P.E. Cantonwine, Strength of thermally exposed alumina fibers Part I Single filament behavior, J. Mater. Sci. 38 (2003) 461–470.
[59] A. Rosenflanz, M. Frey, B. Endres, T. Anderson, E. Richards, C. Schardt, Bulk glasses and ultrahard nanoceramics based on alumina and rare-earth oxides, Nature 430 (2004) 761–764, https://doi.org/10.1038/nature02729.
[60] T. Laha, K. Balani, A. Agarwal, S. Patil, S. Seal, Synthesis of nanostructured spherical aluminum oxide powders by plasma engineering, Metall. Mater. Trans. A 36 (2005) 301–309.
[61] T. Chraska, K. Neufuss, J. Dubsky, P. Ctibor, M. Klementova, Fabrication of bulk nanocrystalline ceramic materials, J. Therm. Spray Technol. 17 (2008) 872, https://doi.org/10.1007/s11666-008-9241-x.
[62] H.-J. Kim, Y.J. Kim, Amorphous phase formation of the pseudo-binary Al2O3–ZrO2 alloy during plasma spray processing, J. Mater. Sci. 34 (1999) 29–33, https://doi.org/10.1023/A:1004492919174.
[63] A.F. Gualtieri, Accuracy of XRPD QPA using the combined Rietveld–RIR method, J. Appl. Crystallogr. 33 (2000) 267–278, https://doi.org/10.1107/S002188989901643X.
[64] T. Chraska, Z. Pala, R. Mušálek, J. Medřický, M. Vilémová, Post-treatment of plasma-sprayed amorphous ceramic coatings by spark plasma sintering, J. Therm. Spray Technol. 24 (2015) 637–643, https://doi.org/10.1007/s11666-015-0225-3.
[65] D. Tabor, The Hardness of Metals, Clarendon Press, Oxford, 1951.
[66] G. Žagar, V. Pejchal, M. Kissling, A. Mortensen, On the Diametric Compression Strength Test of Brittle Spherical Particles, 2017 in preparation.
[67] J.P. Klein, M.L. Moeschberger, Survival Analysis: Techniques for Censored and Truncated Data, second ed., Springer, New York, 2003.
[68] J.J. Mecholsky, R.W. Rice, S.W. Freiman, Prediction of fracture energy and flaw size in glasses from measurements of mirror size, J. Am. Ceram. Soc. 57 (1974) 440–443, https://doi.org/10.1111/j.1151-2916.1974.tb11377.x.
[69] G.K. Bansal, W.H. Duckworth, Fracture stress as related to flaw and fracture mirror sizes, J. Am. Ceram. Soc. 60 (1977) 304–310.
[70] S.R. Choi, J.P. Gyekenyesi, Crack branching and fracture mirror data of glasses and advanced ceramics. National Aeronautics and Space Administration, Lewis Research Center, Cleveland, Ohio, 1998. https://ntrs.nasa.gov/search.

jsp?R=19980137602. (Accessed 12 April 2017).
[71] F.Y. Cui, R.P. Vinci, A chevron-notched bowtie micro-beam bend test for fracture toughness measurement of brittle materials, Scr. Mater 132 (2017) 53–57, https://doi.org/10.1016/j.scriptamat.2017.01.031.
[72] M.G. Mueller, V. Pejchal, G. Žagar, A. Singh, M. Cantoni, A. Mortensen, Fracture toughness testing of nanocrystalline alumina and fused quartz using chevron-notched microbeams, Acta Mater. 86 (2015) 385–395, https://doi.org/10.1016/j.actamat.2014.12.016.
[73] G. Žagar, V. Pejchal, M.G. Mueller, L. Michelet, A. Mortensen, Fracture toughness measurement in fused quartz using triangular chevron-notched micro-cantilevers, Scr. Mater 112 (2016) 132–135, https://doi.org/10.1016/j.scriptamat.2015.09.032.
[74] R.W. Rice, Pores as fracture origins in ceramics, J. Mater. Sci. 19 (1984) 895–914, https://doi.org/10.1007/BF00540460.
[75] H. Schneider, R.X. Fischer, J. Schreuer, Mullite, Crystal structure and related properties, J. Am. Ceram. Soc. 98 (2015) 2948–2967, https://doi.org/10.1111/jace.13817.
[76] I.A. Aksay, D.M. Dabbs, M. Sarikaya, Mullite for structural, electronic, and optical applications, J. Am. Ceram. Soc. 74 (1991) 2343–2358, https://doi.org/10.1111/j.1151-2916.1991.tb06768.x.
[77] H. Schneider, J. Schreuer, B. Hildmann, Structure and properties of mullite—a review, J. Eur. Ceram. Soc. 28 (2008) 329–344, https://doi.org/10.1016/j.jeurceramsoc.2007.03.017.
[78] E. Rocha-Rangel, S. Díaz-de-la-Torre, M. Umemoto, H. Miyamoto, H. Balmori-Ramírez, Zirconia–mullite composites consolidated by spark plasma reaction sintering from zircon and alumina, J. Am. Ceram. Soc. 88 (2005) 1150–1157, https://doi.org/10.1111/j.1551-2916.2005.00234.x.
[79] P. Kumar, M. Nath, A. Ghosh, H.S. Tripathi, Synthesis and characterization of mullite–zirconia composites by reaction sintering of zircon flour and sillimanite beach sand, Bull. Mater. Sci. 38 (2015) 1539–1544.
[80] Q.-M. Yuan, J.-Q. Tan, Z.-G. Jin, Preparation and properties of zirconia-toughened mullite ceramics, J. Am. Ceram. Soc. 69 (1986) 265–267, https://doi.org/10.1111/j.1151-2916.1986.tb07422.x.
[81] F. Deléglise, M.H. Berger, A.R. Bunsell, Microstructural evolution under load and high temperature deformation mechanisms of a mullite/alumina fibre, J. Eur. Ceram. Soc. 22 (2002) 1501–1512, https://doi.org/10.1016/S0955-2219(01)00461-7.